Neutron-skin effect in the nuclear reactions ^{58}Ni+^{122}Sn and ^{64}Ni+^{116}Sn around 6 MeV/nucleon

V. Roberfroid, Y. El Masri, J. Cabrera, Th. Keutgen, L. Lebreton, I. Tilquin, C. Dufauquez, A. Ninane, and J. Van Mol
FNRS and Institute of Nuclear Physics, University catholique of Louvain, 1348 Louvain-la-Neuve, Belgium

R. Régimbart
Laboratoire de Physique Corpusculaire, IN2P3, CNRS/ISMRA, F-14050 Caen Cedex, France

R. J. Charity
Department of Chemistry, Washington University, St. Louis, Missouri 63130, USA

J. B. Natowitz
Cyclotron Institute, Texas A&M University, College Station, Texas 77845, USA
(Received 14 August 2003; published 26 April 2004)

The use of two proton-magic nuclei for both the projectile ($Z=28$) and the target ($Z=50$) in the "mirror" reaction types ^{58}Ni+^{122}Sn and ^{64}Ni+^{116}Sn, leading to the same ^{180}Pt compound nucleus, allows isolation of possible neutron-skin effects from both the target and the projectile. In these reactions, we studied the influence of neutron effects on the competition between fusion-fission, fusion-evaporation, and light-particle emission at equal compound-nucleus excitation energies and similar angular momentum distribution. The comparison of the experimental data, cross sections, and light-particle multiplicities, with the dynamical model HICOL and the statistical model GEMINI incorporating simple aspects of the dynamics, provides insights to the mechanisms of the studied reactions. Our study confirms that, at energy about 6 MeV/nucleon, there is no influence of the entrance channel on the formation and on the decay of the compound nucleus produced by these reactions.

DOI: 10.1103/PhysRevC.69.044611 PACS number(s): 25.70.Jj, 25.85.Ge

I. INTRODUCTION

It has been proposed that in order to produce nuclei far of the valley of stability one should utilize reactions induced by nuclei having "neutron skins" [1]. Indeed, it is generally recognized that some nuclei, such as ^{64}Ni and ^{122}Sn, which are proton magic and neutron-rich, have a neutron skin [2–4]. The effect of such a skin has been extensively studied in the Ni+Sn systems for energies above and below the fusion barrier. The cross sections of fusion-evaporation, fusion-fission, and thus total fusion have been measured [5–7], and the nucleon transfer mechanism has also been extensively studied for these systems [8–11].

From these investigations, it appears that there is a significant decrease in the effective Coulomb barriers for collisions induced by neutron-rich isotopes such as ^{64}Ni or ^{122}Sn at near-barrier energies and thus an increase of the fusion-evaporation cross sections [5]. It also seems that the neutron exchange is larger and faster using these nuclei to equilibrate the N/Z ratio.

The first goal of this paper is to determine any eventual advantage of using a neutron-rich projectile ^{64}Ni on ^{116}Sn at around 6 MeV/nucleon to produce a ^{180}Pt compound nucleus (CN) compared to the ^{58}Ni+^{122}Sn entrance channel. The second goal of this paper is to analyze the influence of the entrance channel on the CN decay. Therefore, in order to isolate any neutron-skin effect, the beam energies for the two entrance channels were chosen to produce the ^{180}Pt CN either at equal excitation energy ($E^* \simeq 122$ MeV) or with similar angular momentum distribution.

For this purpose, the reactions ^{58}Ni+^{122}Sn at 375.5 and 354 MeV and ^{64}Ni+^{116}Sn at 382.5 MeV were investigated. We measured the cross sections for fusion-evaporation, fusion-fission, and thus total fusion, and the multiplicities of the emitted neutrons, protons, and α particles [12]. Using this set of data, we have compared our results with the calculations of two simulation codes: HICOL (a dynamical model) [13] and GEMINI (a statistical model) [14].

The paper is organized as follows: in Sec. II the experimental setup is briefly described. In Sec. III we discuss the analysis procedures and the subsequent results. In Sec. IV we compare our results with simulations followed by a short summary in Sec. IV.

II. EXPERIMENTAL SETUP

The experiments were carried out at CYCLONE, the Louvain-la-Neuve cyclotron accelerator. The reactions studied were: ^{58}Ni+^{122}Sn at 375.5 (b375) and 354 MeV (b354) and ^{64}Ni+^{116}Sn at 382.5 MeV (b382) Ni beams bombarding energies. Self-supporting ^{122}Sn and ^{116}Sn targets with thicknesses about 280 μg/cm^2 were used. Figure 1 displays a schematic view of the in-plane experimental setup. The detection systems consisted of the following:

(1) Two large-area position-sensitive, X and Y, multiwire proportional gas counters (MWPC1,2) to detect and characterize the fission fragments (FF). They were positioned at 29.5 cm from the target and at a central angle of 50° on each side of the beam axis. These detectors contain two planes of 162 horizontal and 156 vertical, 20 μm diameter, gold-plated tungsten wires separated by a double-faced aluminized mylar foil held at a potential of −560 V. The wire positions are

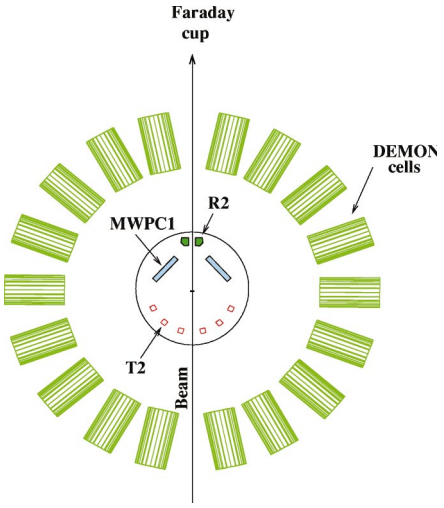

FIG. 1. (Color online) Schematic view of the in-plane experimental setup.

read through a high precision semiconductor delay lines. These structures are contained in a airtight enclosure in which isobutane gas circulates continually and are maintained at a constant pressure of 7.5 mbar. The entrance and outlet faces of these detectors were made from 2.5 μm thick aluminized mylar foils held at ground potential. The detectors, covering 20×20 cm^2 active surface, measure the X and Y positions and the time of flight of fission fragments, detected in coincidence, with a time resolution about 500 ps. From these measurements, the angular positions θ and ϕ with respect to the beam axis are determined with an angular resolution of 0.4°. Based on the linear-momentum conservation law and assuming the mass of the fissioning nucleus, the energies and the masses of the two coincident ions are calculated event by event. Following this procedure and taking account the time resolution of the beam structure (1.5 ns), the uncertainties for the fragments energy losses in the target thickness (10%), and the detection angular resolution (0.4°), the systematic errors on the fission fragment masses were estimated to 6%.

(2) Two micro-channel-plate-Si detector assemblies ($R1,R2$) were used to detect and characterize fission fragments and evaporation residues (ER). Each of these detectors consists of two of microchannel plates with two Si ($\Delta E,E$) counters of 380 mm^2 active area. They were placed at 62 cm from the target and at ±7° angles on each side of the beam axis (with a detection opening angle of about 1°). The electrons, detected by the microchannel plates, were produced in a 500 Å thick Au layer deposited on the entrance surface of the ΔE Si detectors. These detectors measure the time of flight, with a time resolution around 700 ps [full width at half maximum (FWHM)], and the energy of the detected ions to be deduced with a resolution of 50 keV. The pulse-height defects in the Si detectors were obtained using the formalism of Kaufman *et al.* [15] fitted to the measured spectrum of ^{252}Cf fission fragments.

(3) Six triple-Si telescopes ($T1-T6$), positioned at backward angles (±115°, ±140°, and ±165°), detected and characterized light charged particles (LCP). They were set at a distance of 19.5 cm from the target. Each telescope was composed of three silicon counters with thicknesses of 85 μm, 706 μm, and 706 μm, respectively. The particle identification and their total energies were determined from the energy deposition and/or the energy loss measurements (ΔE_1, ΔE_2 and ΔE_3).

(4) 96 DEMON neutron counters each with an active volume of 16 cm diameter and 20 cm thickness were located outside of the reaction chamber. They were mounted on a large *A*l sphere of 4 m diameter located 5 m above the ground to minimize the scattered neutron background. Each cylindrical DEMON cell is filled with NE213 liquid organic scintillator and is coupled to a 5-in. photomultiplier (PM XP4512B). These detectors were positioned in a 4π geometry at a 1.85 m distance from the target as seen in Fig. 3 of Ref. [16]. The determination of the neutron intrinsic detection efficiency as a function of energy and electronic threshold are discussed in Ref. [17].

For all the detectors used in this experimental setup, the time of flight was started by the cyclotron radio frequency. The time stability of this reference was continuously controlled using the γ-ray peak in the DEMON counters and which was detected with a time resolution better than 2.5 ns (FWHM).

The constant T^0 values of the zero time of flights required for all the detected particles and ions in these experiments were extracted either from the elastic scattering events or from the γ-ray peaks (neutrons). The uncertainty on these values were about 1.5 ns mainly due to the time resolution of the beam structure.

Neutrons and LCP (p and α) were detected in coincidence with FF and ER. Unfortunately, due to the very small solid angle sustained by the $R1$, $R2$ detector assemblies and the beam time allocated for these experiments, the number of light particles detected in coincidence with ER was too low to undertake a study of their properties. The target holder was set at +18 keV potential for secondary electron suppression. The beam was stopped in a well shielded beam dump located ≃6 m downstream from the target. The Faraday cup, used to read the beam current, was coupled to an electron repeller set at −1 kV potential.

The reactions b375 and b382 were later studied without DEMON detectors. These two additional experiments, designated d375 and d382 in the remainder of this report, were used to determine the angular distributions $d\sigma/d\Omega$ of the fission fragments and the evaporation residues. Hence the detectors $R1$ and $R2$ were moved to sample the angles between ±7° and ±11°.

III. ANALYSIS PROCEDURES AND RELATED RESULTS

A. Properties of the evaporation residues and fission fragments determined with the *R*1 and *R*2 detectors

To isolate FF and ER from the other particles collected by the $R1$ and $R2$ detectors, selections on the two-dimensional plot of the time of flight versus kinetic energy were employed. Examples of the selections used, are shown in Fig.

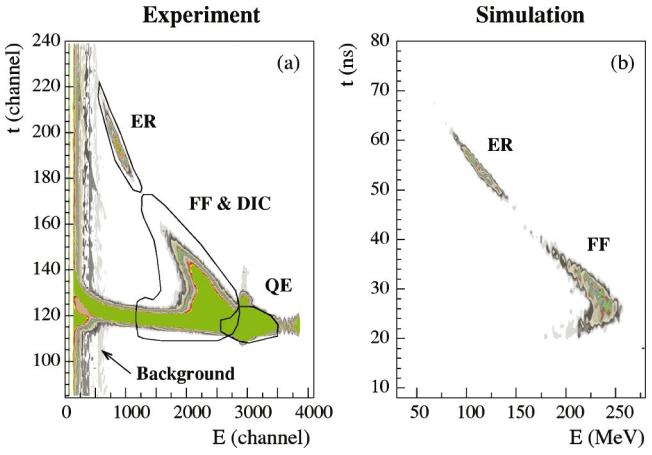

FIG. 2. (Color online) Experimental (a) and simulated (b) bidimensional plots of time of flight vs energy of the reaction products collected in the detector $R1$ or $R2$ in the ^{58}Ni(375.5 MeV)+^{122}Sn reaction. The two-dimensional gates used to experimentally select evaporation residues, fission fragments and deep-inelastic collisions, and quasielastic scattering are indicated in panel (a).

2(a) for the data collected in the b375 reaction. Figure 2(b) displays the results predicted by the GEMINI code for the same reaction [14]. Both figures are in good agreement. However experimentally, while the ER events are very well separated from the other reaction products, the FF are mixed with the events of quasielastic (QE) and deep inelastic collisions (DIC).

To determine the fusion-evaporation cross section σ_{er} a Monte Carlo code was used to reproduce the experimental ER velocity distributions $d^2\sigma_{er}/d\Omega dv_{er}$ at $\theta_{lab} \simeq 7°$, observed in the b375 and b382 runs. This code is based on the form assumed by Morgenstern [18]:

$$\frac{d^2\sigma_{er}}{d\Omega dv_{er}} = Kv_{er}^2 \exp\left(-\frac{[v_{er} - v_{cn}\cos(\theta)]^2}{2S^2}\right) \times \exp\left(-\frac{v_{cn}^2 \sin^2(\theta)}{2S^2}\right), \quad (1)$$

where v_{er} and v_{cn} are the velocity in the laboratory frame of the ER and the CN, respectively. The value of v_{cn} was set to the reaction center-of-mass velocity as expected for complete fusion. This code convolutes Eq. (1) with the effects of the target thickness on the angular and the energy stragglings and the effect of the beam time resolution ($\simeq$1.5 ns FWHM) which induce an important spreading in the velocity distributions. The only free parameters in the code were K and S which were adjusted to obtain the best fit to the experimental data. The results of these fits are displayed in Fig. 3.

The fusion-evaporation cross sections are determined from the resulting values of K and S as

$$\sigma_{er} = (2\pi)^{3/2} K S^3. \quad (2)$$

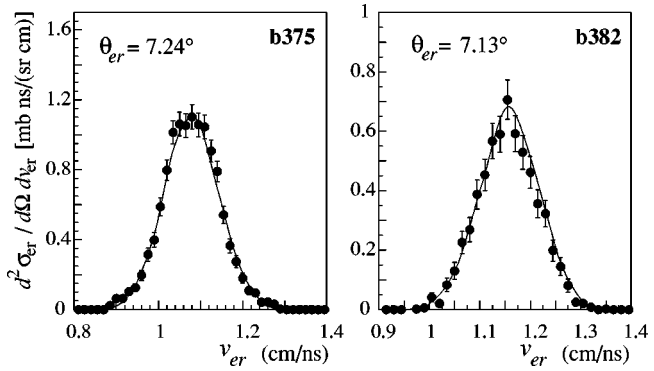

FIG. 3. Fits (solid curve) of the experimental ER velocity distributions (data points with the corresponding statistic errors), in b375 and b382 experiments, by a Monte Carlo code based on Eq. (1) in order to determine the parameters K and S needed for the evaluation of the σ_{er} cross sections.

In the d375 and d382 experiments, the angles of the detectors $R1$ and $R2$ were moved to angles of +7°, −7.5°, +8°, −8.5°, +9°, and −10.5° with respect to the beam axis. This allowed the determination of the angular distribution $d\sigma_{er}/d\Omega$ of the ER and the angular distribution $d\sigma_f/d\Omega$ of the FF, respectively.

Figure 4(a) presents the experimental angular distribution $d\sigma_{er}/d\Omega$ (in the laboratory frame) of the ER (data points) determined in the d375 experiment. The full curve does not result from a fit to the data points, but results from the Monte Carlo code with the K and S input parameters extracted from the ER velocity distribution adjustment as shown in Fig. 3. However, one observes a good agreement.

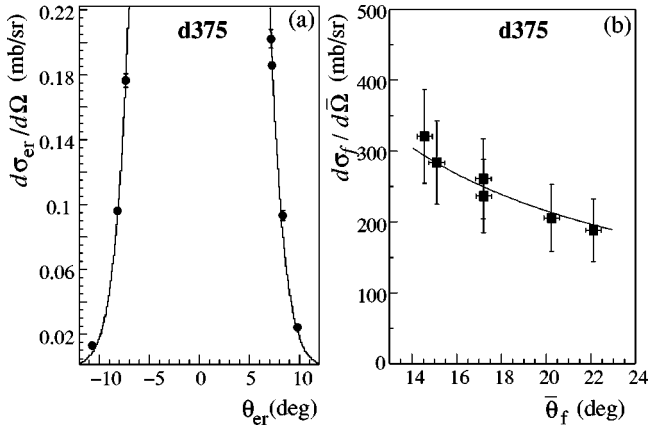

FIG. 4. (a) Experimental angular distribution of the ER (data points) as a function of the detection angles (in the laboratory frame) in the d375 experiment and the predicted result (full curve) using the values of the parameters K and S extracted from the ER velocity distributions (Fig. 3). (b) Experimental angular distribution of the FF (data points) in the center-of-mass frame in the d375 experiment and the results of the fit by a $K/\sin(\bar{\theta}_f)$ type function where $\bar{\theta}_f$ is expressed in the center-of-mass frame.

TABLE I. Experimental cross sections of fusion-evaporation σ_{er}, fusion-fission σ_f, and total fusion $\sigma_{fusion}=\sigma_{er}+\sigma_f$. The values ℓ_{crit} are the corresponding critical angular nomenta extracted from the experimental or theoretical σ_{fusion} assuming the sharp cut-off approximation: $\sigma_{fusion=}\pi\lambda^2(\ell_{crit}+1)^2$. The theoretical values ℓ_{crit} are based on the static fusion model of Wilcke [19]. For comparison, are also listed the anuglar momenta $\ell_{Bf=0}$ at which ^{180}Pt fission barrier is predicted to vanish in the calculations of Sierk [20].

Reaction	σ_{er}(mb)	σ_f (b)	σ_{fusion}(b)	ℓ_{crit} Experimental	ℓ_{crit} Static model	$\ell_{Bf=0}$ ($\hbar$)
^{58}Ni+^{122}Sn at 375.5 MeV	50±5	1.45±0.13	1.50±0.14	150$\hbar$	111$\hbar$	72$\hbar$
^{64}Ni+^{116}Sn at 382.5 MeV	50±8	1.40±0.13	1.45±0.14	149$\hbar$	120$\hbar$	72$\hbar$

Figure 4(b) presents the center-of-mass angular distribution $d\sigma_f/d\overline{\Omega}$ of the FF observed in the d375 experiment. The experimental data (filled squares) are fitted by the function:

$$\frac{d\sigma_f}{d\overline{\Omega}}=\frac{K}{\sin(\overline{\theta_f})}, \tag{3}$$

where $\overline{\theta_f}$ is the center-of-mass emission angle of the FF and K is the fit parameter. The fusion-fission cross section σ_f is determined as:

$$\sigma_f=2\pi^2K. \tag{4}$$

The uncertainties on $d\sigma_f/d\overline{\Omega}$ are larger than for the ER distribution $d\sigma_{er}/d\Omega$ because of the conversion to the center-of-mass frame. To these errors, uncertainties were added to take into account the difficulty to isolate fission from DIC and QE events.

The extracted values of σ_f, σ_{er}, and $\sigma_{fusion}=\sigma_f+\sigma_{er}$ are listed in Table I for the reactions studied in this work. The errors on σ_{er} correspond to the maximum difference between the values calculated using the extreme values of the input parameters K and S in the Monte Carlo code which generate an ER velocity distribution within the error bars (statistical and systematic errors) on the data points. The experimental values σ_{er} are in agreement with the reported data by Freeman *et al.* [5]. In contrast, the extrapolation of the experimental values of σ_f as reported by Lesko [6] and Wolfs [7] at our beam energy domain seems to be lower than ours and more in agreement with fusion static models (see Table I). This is due to our difficulty to separate fission, DIC and QE in our experimental results.

Table I also displays ℓ_{crit}, the maximum ℓ wave involved in the complete-fusion processes. These values are estimated from either the experimental or the theoretical σ_{fusion} values, assuming the sharp cut-off approximation, i.e, $\sigma_{fusion}=\pi\lambda^2(\ell_{crit}+1)^2$. In Table I, the theoretical values of ℓ_{crit} are calculated using the static fusion model of Wilcke [19]. Also listed are the angular momenta $\ell_{Bf=0}$ at which the ^{180}Pt fission barrier is predicted to vanish in the calculations of Sierk [20]. The large values of the theoretical and experimental ℓ_{crit}, as compared to $\ell_{Bf=0}$, clearly suggest the presence of another reaction mechanism i.e., contributions from fast fission [21] or completely relaxed DIC. Similarly, the difference between the calculated and the experimental ℓ_{crit} values originates from the mixing of fusion-fission and deep inelastic events as shown in Fig. 2(a). This is the reason why experimental values of ℓ_{crit} and σ_{fusion} could not be used as input parameters in any statistical model (like GEMINI). This is in contrast to the study performed in our recently published work [16]. The input parameters used are discussed in Sec. IV A.

B. Properties of the fission fragments measured with the detectors MWPC1, 2

From the measured masses and velocities of the two FF detected in coincidence in the two MWPC, the total kinetic energy (TKE) in the center-of-mass frame could be estimated. To separate fission from other processes, a two-dimensional plot of TKE versus the FF mass was used as shown in Fig. 5. The events in the two "ears" shaped regions in this figure correspond to the elastic and quasielastic reaction products while the events in the "head" are associated with fission and deep inelastic processes which are indistinguishable. Indeed, even the correlations between the polar angles θ_{f1} of the FF1 detected in the MWPC1 and the angles θ_{f2} of the coincident FF2 detected in the MWPC2 do not allow one to separate the DIC and the fission processes. To

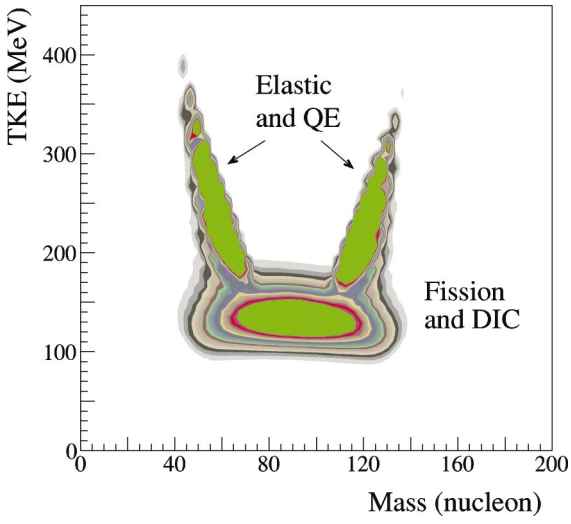

FIG. 5. (Color online) Evolution of TKE as a function of the mass of the reaction products detected in the MWPC1 in the b375 experiment. One can clearly identify the contributions of the different reaction processes resulting from ^{58}Ni(375.5 MeV)+^{122}Sn reaction.

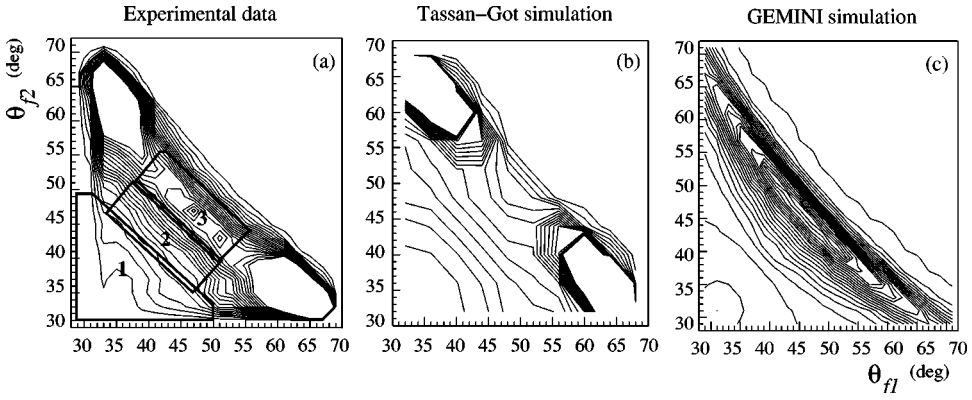

FIG. 6. (a) Experimental correlation between θ_{f1} and θ_{f2} fission fragments polar angles as observed by the MWPCs in the ^{58}Ni + ^{122}Sn at 375.5 MeV reaction; (b) identical simulations using Tassan-Got and Stéfan code [22] for QE and DIC events; (c) similar simulations using GEMINI code for conventional fission.

illustrate this, Fig. 6(a) presents this experimental correlation (θ_{f2} vs θ_{f1}) for the angular region covered by the two MWPCs in the reaction ^{58}Ni(375.5 MeV) + ^{122}Sn. Figure 6(b) displays the identical results for the DIC and the QE events as predicted by the simulation using the Tassan-Got and Stéfan code [22]. Figure 6(c) displays similar results for the conventional fission as predicted by the GEMINI code (described in Sec. IV B). It appears that it is indeed impossible to find any angular region (θ_{f1}, θ_{f2}) where the fission is completely isolated from DIC process, in contrast to the QE. Three regions designated by the numbers 1, 2, and 3 are shown in Fig. 6(a) and their corresponding events are displayed on the TKE vs A_{f1} correlations in Fig. 7. It is noted that the events of region 1, whose FFs are emitted at rather forward angles, are associated with intense asymmetric mass partition processes with mean TKE values similar to the fission ones. It also appears that, the more one approaches the center of the MWPCs, the more the mass partition becomes symmetric but with a wide mass distribution.

In order to determine the intrinsic detection efficiency of the two MWPCs, we calculated the ratio of the experimental differential cross section $d\sigma_{elastic}/d\Omega$ to the value expected for the Rutherford scattering $d\sigma_{Ruth}/d\Omega$ at the different detection angles in the MWPCs. These ratios were found to be of 75 to 80% for angles smaller than 34° and decrease as the detection angle increases, illustrating the presence of inelastic processes.

The cross sections for fusion-fission σ_f were determined by applying the same method that was used for the detectors $R1$ and $R2$, i.e., by adjusting the angular distribution $d\sigma_f/d\Omega$ in the center-of-mass frame by a $K/\sin(\theta_f)$ function as shown in Fig. 8. The resulting σ_f values, which are not corrected by the intrinsic detection efficiency, are listed in Table II. The MWPC efficiencies, also listed in Table II, are determined through the ratios of σ_f calculated from the MWPCs (Table I) and σ_f calculated from the $R1$ and $R2$ detectors (Table I). The resulting efficiencies are similar to the values extracted from the elastic-scattering $d\sigma_{elastic}/d\sigma_{Ruth}$ data discussed previously.

C. Results from the DEMON detectors

Two types of radiation can pass through the reaction chamber wall and be detected by the DEMON cells; γ rays and neutrons. To separate these two radiations, a "pulse-shape discrimination" technique has been utilized. The integrated slow (Q_s) and the total (Q_t) parts of the light-output signal delivered by each detector were correlated in a two-dimensional plot as displayed in Fig. 9. The neutron kinetic-energy spectra were constructed from the neutron times of flight with the appropriate correction for the energy-dependent intrinsic detection efficiencies of the DEMON detectors [17]. The energy spectra $d^2\nu_n/d\Omega dE_n$ were fitted as-

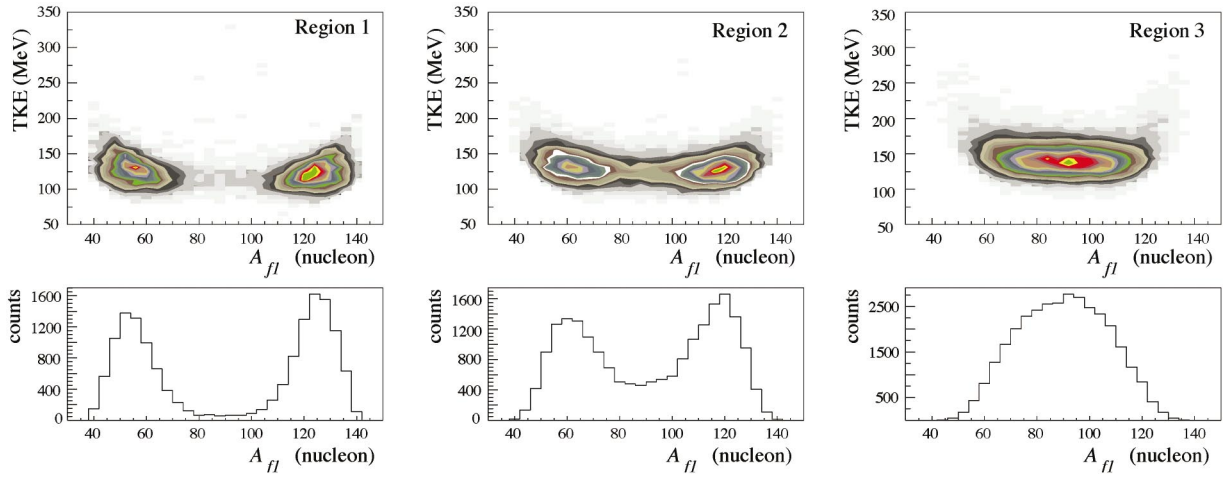

FIG. 7. (Color online) TKE vs A_{f1} correlations and their projections on the A_{f1} axis for the different angular selections (1,2,3) shown in Fig. 6(a).

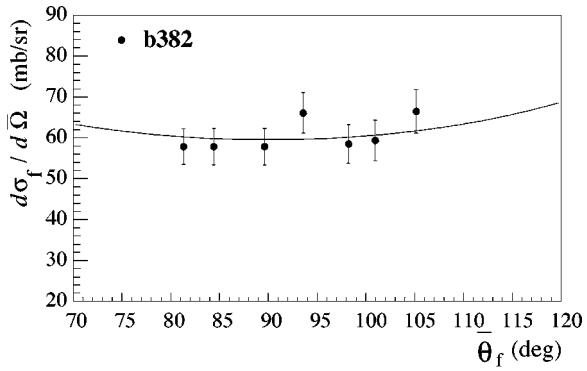

FIG. 8. Fit of FF angular distribution $d\sigma_f/d\bar{\Omega}$ in the center-of-mass frame by a $K/\sin(\bar{\theta}_f)$ function type in the reaction b382 observed in the MWPC detectors.

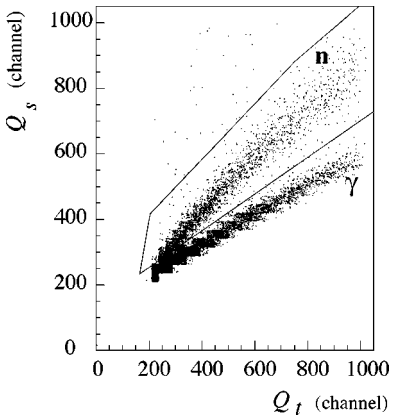

FIG. 9. Discrimination of n-γ in a DEMON detector using pulse-shape analysis of the light-output signal.

suming contributions from three sources; prescission neutrons emitted by the CN before fission and postscission emissions from the two fission fragments FF1 and FF2. The prescission spectrum corresponding to neutrons emitted from the CN was assumed to be of a "surface" type Maxwellian distribution [16], and its expression in the laboratory system is

$$f_S(T_n,\nu_n) = \frac{\nu_n}{4\pi T_n^2}\bar{E_n}\sqrt{\frac{E_n}{\bar{E_n}}}e^{-E_n/T_n}. \quad (5)$$

The postscission spectrum corresponding to emissions from the fission fragments was assumed to be of a "volume" type Watt distribution [16,23], and its expression in the laboratory system is

$$f_V(T_n,\nu_n) = \frac{\nu_n}{2(\pi T_n)^{3/2}}\sqrt{E_n}e^{-E_n/T_n}. \quad (6)$$

In these equations, ν_n and T_n are the multiplicities and the nuclear temperatures associated with the respective emitting sources; E_n and $\bar{E_n}$ are the neutron energies in the laboratory and in the center-of-mass frames, respectively. Thus the function used to fit the energy distributions of neutrons detected in coincidence with the two FF in the MWPCs was:

$$\frac{d^2\nu_n}{d\Omega dE_n} = f_V(T_n^{f1},\nu_n^{f1}) + f_V(T_n^{f2},\nu_n^{f2}) + f_S(T_n^{cn},\nu_n^{cn}). \quad (7)$$

T_n^{f1} and ν_n^{f1} are the nuclear temperature and the associated neutron multiplicity of the FF detected in the MWPC1 (postscission parameters). T_n^{f2} and ν_n^{f2} are the nuclear temperature and the associated neutron multiplicity of the FF detected in the MWPC2 (postscission parameters). T_n^{cn} and ν_n^{cn} are the nuclear temperature and the associated neutron multiplicity of the CN (not detected and assumed to recoil along the beam axis) (prescission parameters).

These six parameters are first determined by fitting the neutron experimental energy spectra $d^2\nu_n/d\Omega dE_n$ for the whole set of DEMON detectors. However, the number of free parameters was reduced assuming that the temperatures of the two FF were equal ($T_n^{f1}=T_n^{f2}$), as expected for a thermally equilibrated fissioning nucleus. It should be noted that no preequilibrium contribution was observed in these experiments.

Subsequently, in a second step, the temperatures were held fixed and the multiplicities were refined by fitting the neutron angular distributions $d\nu_n/d\Omega$ in and out of the reaction plane by the following expression:

$$\frac{d\nu_n}{d\Omega}_{E_s} = \int_{E_s}^{\infty} f_V(T_n^{f1},\nu_n^{f1})dE + \int_{E_s}^{\infty} f_V(T_n^{f2},\nu_n^{f2})dE + \int_{E_s}^{\infty} f_S(T_n^{cn},\nu_n^{cn})dE, \quad (8)$$

where E_s is the neutron energy threshold, imposed on each experimental neutron spectrum, which was set to $E_s=2$ MeV. Note that in our setup, neutrons and γ rays were already well discriminated above 1.25 MeV threshold. Figure 10(a) compares the experimental energy distribution $d^2\nu_n/d\Omega dE_n$ and the calculated final fit for a detector positioned at $\theta_n=50°$ and $\phi_n=0°$ and $\phi_n=180°$. Figure 10(b) shows the corresponding comparison for the angular distribution $d\nu_n/d\Omega$ of 12 DEMON detectors positioned in the reaction plane $\phi_n=0°$. In these figures, the dashed lines represent the prescission contribution from the CN and the dotted and dashed-dotted lines are the postfission components associated with the FF1 and FF2, respectively. The thick solid lines represent the sum of all these contributions and this should be compared to the experimental data (open and black data points, respectively).

TABLE II. Experimental fusion-fission σ_f cross sections resulting from the MWPC detectors data and their deduced mean detection efficiency in the two studied reactions.

Reaction	σ_f (b)	Efficiency
^{58}Ni+^{122}Sn at 375.5 MeV	1.09±0.04	75±10%
^{64}Ni+^{116}Sn at 382.5 MeV	1.18±0.04	80±10%

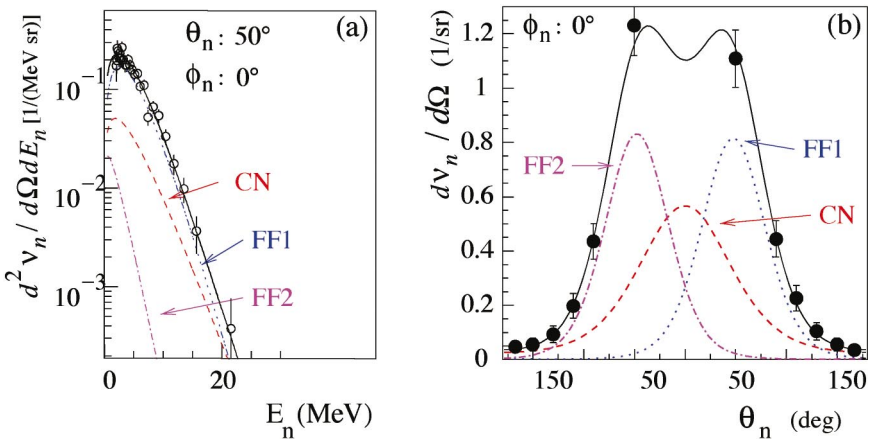

FIG. 10. (Color online) Examples of fits to a neutron kinetic-energy spectrum $d^2\nu_n/d\Omega dE_n$ (a) and to the angular distribution $d\nu_n/d\Omega$ (b) measured in the b375 reaction (see text for details). Neutron energies are considered in the laboratory frame.

From these figures, one observes that the CN emissions are focused to forward angles and that the FF contributions dominate at angles $\theta_n = \pm 50°$, around the central angular positions of the two MWPC.

Figure 11 presents the evolution of the fitted neutron multiplicities and the nuclear temperatures for the three emitting sources (CN, FF1, and FF2) as a function of the mass A_{f1} of FF1, in the reactions ^{58}Ni+^{122}Sn at 354 MeV and ^{64}Ni +^{116}Sn at 382.5 MeV. It should be noted that the temperatures of the FF and the CN obtained in the fits remain essentially constant for all studied mass asymmetries. This observation justifies the assumption that the CN is thermodynamically equilibrated prior to scission. One can also observe a constant increase of the FF1 multiplicities ν_n^{f1} with its mass A_{f1}. For a constant temperature process, the excitation energy U of the emitting nucleus is expected to be proportional to its mass A as illustrated in the following expression:

$$U = a_n T^2 = \frac{A}{a_0} T^2, \tag{9}$$

where a_n is the level-density parameter which can vary from $A/7$ to $A/11$ MeV^{-1} as a function of nuclear temperatures [24].

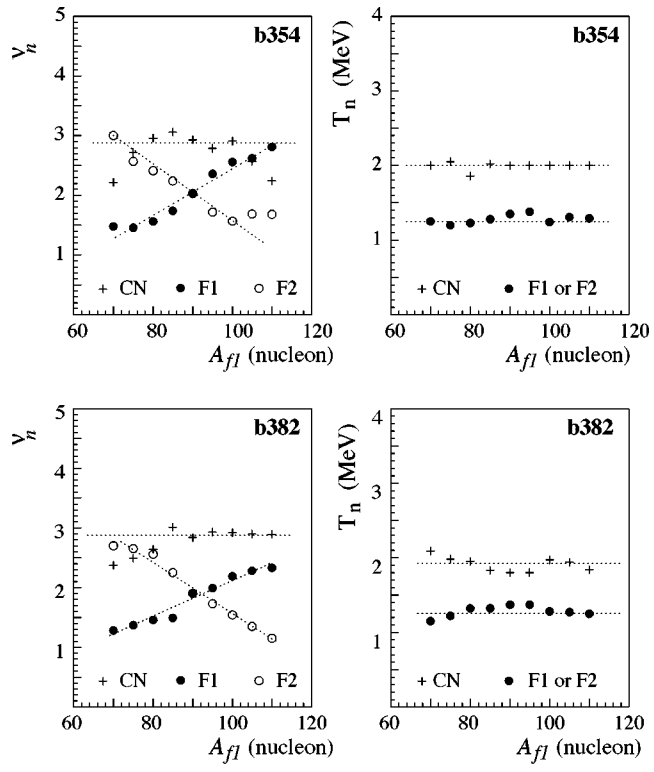

FIG. 11. Evolutions of ν_n^{cn}, ν_n^{f1}, and ν_n^{f2}, the experimental neutron prescission and postscission multiplicities and the corresponding nuclear temperatures T_n^{cn}, T_n^{f1}, and T_n^{f2}, in the reactions ^{58}Ni +^{116}Sn at 354 MeV (b354) and ^{64}Ni+^{116}Sn at 382.5 MeV (b382), as a function of the FF1 mass A_{f1}. The dotted lines are to guide the eye.

One can also observe in Fig. 11 that the CN multiplicities ν_n^{cn} are quite independent from the mass A_{f1}. But it seems, nonetheless, that ν_n^{cn} decreases for very asymmetric mass partitions and especially in the ^{58}Ni+^{122}Sn experiment. This may result from the important mixing of fission events with other inelastic processes such as quasielastic which have a larger presence in the ^{58}Ni+^{122}Sn experiment for kinematic reasons. Table III lists the multiplicities and nuclear temperatures for symmetric mass partition ($A_{f1} = (A_{cn}/2) \pm 5$ nucleons) events which are less contaminated by other nuclear processes.

We also observe in Table III that the extracted multiplicities and temperatures for the CN and for two the FF are the same, within the error bars, for the two last reactions. In fact, as shown in the first column, these reactions lead to the same CN with the same initial excitation energy ($E^*_{cn} \simeq 123$ MeV) in contrast to the first reaction for which the CN has a higher value ($E^*_{cn} \simeq 139$ MeV).

D. Light charged particles

The discrimination among LCP was achieved using two bidimensional plots: the energy lost in the second Si counter ΔE_2 as a function of the energy lost in the first ΔE_1 and the energy lost in the third counter ΔE_3 as a function of ΔE_2 as shown in Fig. 12. Only α particles and protons were analyzed because the yield of the other LCP was not sufficient to determine their multiplicities with statistical significance.

TABLE III. Initial excitation energies of the ^{180}Pt CN formed in this work. Also listed are the experimental prescission and postscission neutron multiplicities and nuclear temperatures determined for the CN and the FF for a symmetric mass partition.

Reaction	E^*_{cn} (MeV)	ν_n^{cn}	T_n^{cn}(MeV)	$\nu_n^{f1}=\nu_n^{f2}$	$T_n^{f1}=T_n^{f2}$(MeV)
^{58}Ni+^{122}Sn at 375.5 MeV	139	3.2±0.2	1.9±0.1	2.3±0.1	1.4±0.1
^{58}Ni+^{122}Sn at 354 MeV	124	3.0±0.2	2.0±0.1	2.0±0.1	1.4±0.1
^{64}Ni+^{116}Sn at 382.5 MeV	122	3.0±0.2	1.8±0.1	1.9±0.1	1.4±0.1

The energy spectra of protons and α particles in the laboratory system were normalized and fitted with a Coulomb-shifted Maxwellian spectrum:

$$\frac{d^2\nu_{lcp}}{dEd\Omega} = \sum_{i=f1,f2,nc} \frac{\nu^i_{lcp}(\bar{E}-B^i_c)}{4\pi T^{i2}_{lcp}} \sqrt{\frac{\bar{E}}{E}} e^{\left(-(\bar{E}-B^i_c)/T^i_{lcp}\right)}, \quad (10)$$

where E and $\bar{E}$ are the energies of the LCP in the laboratory and center-of-mass frames, respectively, B^i_c are their effective emission barriers. To reduce the number of fitted parameters, ν^i_{lcp} and T^i_{lcp}, we have fixed to the mean CN temperature calculated as

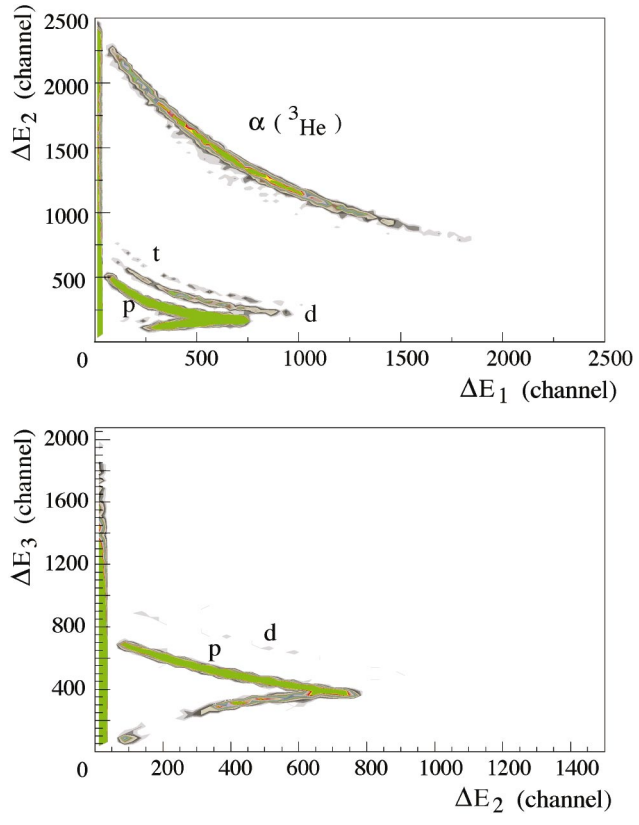

FIG. 12. (Color online) Bidimensional plots showing the discrimination of the different LCP from the correlation of the energy losses in the three Si counters ΔE_1, ΔE_2, and ΔE_3 of each Sitelescope. The plotted data were obtained with the reaction ^{58}Ni + ^{122}Sn at 375.5 MeV.

$$\langle T^{cn}\rangle = \frac{\sum_{\ell=\ell_{er}}^{\ell^{exp}_{crit}} (2\ell+1)T(\ell)}{\sum_{\ell=\ell_{er}}^{\ell^{exp}_{crit}} (2\ell+1)}, \quad (11)$$

where

$$T(\ell) = \sqrt{\frac{a_0}{A_{cn}}\left(E^*_{cn} - \frac{\hbar^2\ell(\ell+1)}{2\Im}\right)} \quad (12)$$

with A_{cn} being the mass of the CN and $\Im$ its momentum of inertia. The value of ℓ_{er} which corresponds to the maximum value of the angular momentum leading to the ER formation is extracted from σ_{er} and ℓ^{exp}_{crit} is taken from Table I.

Moreover, the temperatures and the postscission multiplicities of the two FF, which are free parameters in the fit, were assumed equal over the entire fission mass distribution, i.e., $\nu^{f1}_{lcp}=\nu^{f2}_{lcp}$ and $T^{f1}_{lcp}=T^{f2}_{lcp}$. An analysis of these multiplicities as a function of the fission mass partition was not possible because the large statistical uncertainties.

The emission barriers B^i_c in Eq. (10) were calculated from Vaz and Alexander systematics [25]:

$$B^i_c = \frac{1.44Z_i}{1.18A_i^{1/3}+3.928}(\text{MeV}) \quad \text{for} \quad p \quad (13)$$

$$B^i_c = \frac{2.88Z_i}{1.18A_i^{1/3}+4.642}(\text{MeV}) \quad \text{for} \quad \alpha, \quad (14)$$

where Z_i and A_i are the charge and the mass number of the source nucleus ($i=f1$, $f2$, and CN). However, the best fits of the LCP energy distributions were obtained by lowering by 4 MeV the CN associated barriers of Ref. [25]. Such effects have been already observed in previous studies [26–30] and appear to reflect both increased diffuseness and deformation of the emitters for large angular momenta. Table IV presents the results of the analyses of LCP energy spectra derived from the six Si-detectors T1 to T6. The uncertainties take into account the statistical and systematical errors. The former are large because of the small number of detected LCP.

Moreover, it is important to note that, in our analysis, LCP emission barriers [in Eq. (10)] were maintained constant during the full decay process of the CN. However deformation of the composite system is important in DIC and evolves

TABLE IV. Experimental prescission and postscission LCP nuclear temperatures and multiplicities determined for the compound nucleus and fission fragment sources in the three discussed reactions. The values T_{lcp}^{cn} are calculated following Eqs. (11) and (12) (see text for details).

Reaction	T_{lcp}^{cn} (MeV)	$T_{lcp}^{f1}=T_{lcp}^{f1}$ (MeV)	ν_p^{cn}	$\nu_p^{f1}=\nu_p^{f2}$	ν_α^{cn}	$\nu_\alpha^{f1}=\nu_\alpha^{f2}$
^{58}Ni+^{122}Sn at 375.5 MeV	2.2	1.7	0.28±0.25	0.24±0.15	0.14±0.10	0.16±0.11
^{58}Ni+^{122}Sn at 354 MeV	2.0	1.7	0.16±0.14	0.17±0.10	0.10±0.07	0.06±0.04
^{64}Ni+^{116}Sn at 382.5 MeV	2.0	1.7	0.16±0.14	0.23±0.13	0.11±0.07	0.10±0.07

with time. Thus, the barriers are suspected to substantially decrease allowing LCP to escape with small kinetic energies. For this reason we may have experimentally underestimated the LCP multiplicities.

IV. SIMULATIONS

A. Dynamical calculations

The code HICOL [13] describes, as a function of time, the evolution of the nuclear interactions between the projectile and target during a collision. However, this code does not describe the subsequent decay by fission or the evaporation of an excited nucleus. The reactions simulated by the code, are thus primarily quasielastic and deep-inelastic reactions. Fast fission may be considered in this dynamical code as completely damped DIC with a large number of nucleons exchanged.

HICOL can calculate, amongst different reaction parameters, the TKE and the mass of the final reaction products. Figure 13(a) displays the mass evolution of the reaction products, i.e., the quasitarget and quasiprojectile as a function of the angular momentum. The angular momentum ℓ_{sym}, below which the final mass partition is quasisymmetric ($A_{f1}=90\pm5$ nucleons), is also displayed in Fig. 13(a) and is equal to $100\hbar$. Figure 13(b) represents the evolution of the TKE as a function of the mass of one reaction product corresponding to the ^{58}Ni(375.5 MeV)+^{122}Sn reaction. This figure must be compared with the experimental data in Fig. 5. One can observe that, if one selects the events such as those in the "head" in Fig. 13(b), we select an important contribution of deep inelastic events with angular momenta smaller than $\ell_{hicol}(\simeq 150\hbar)$. Table V lists the cross sections (in barns) of total "fusion" as predicted by HICOL simulations, including the DIC in this selection. The experimental values and the values predicted by the static fusion model of Wilcke [19] are also listed in this table. One can observe a very good agreement between the experiment and the HICOL predictions.

The full squares in the three figures correspond to the region of symmetric mass partition. One can observe in Fig. 13(b) that the completely damped DIC are present in this region. Figure 13(c) displays the evolution of the nuclear deformation (ratio of major to minor axes, see Sec. IV B) of the formed system as a function of the angular momentum ℓ predicted by HICOL. The mean deformation ⟨ratio⟩ of the dinuclear system leading to mass-symmetric reaction products (full square) is equal to 2.4 in these calculations.

B. Statistical-model calculations

The code GEMINI [14] is a statistical Monte Carlo code which simulates the decay of a compound nucleus given with an initial angular momentum and an excitation energy. Although GEMINI cannot predict the cross section of fusion, it can calculate the fusion-evaporation cross section and the pre

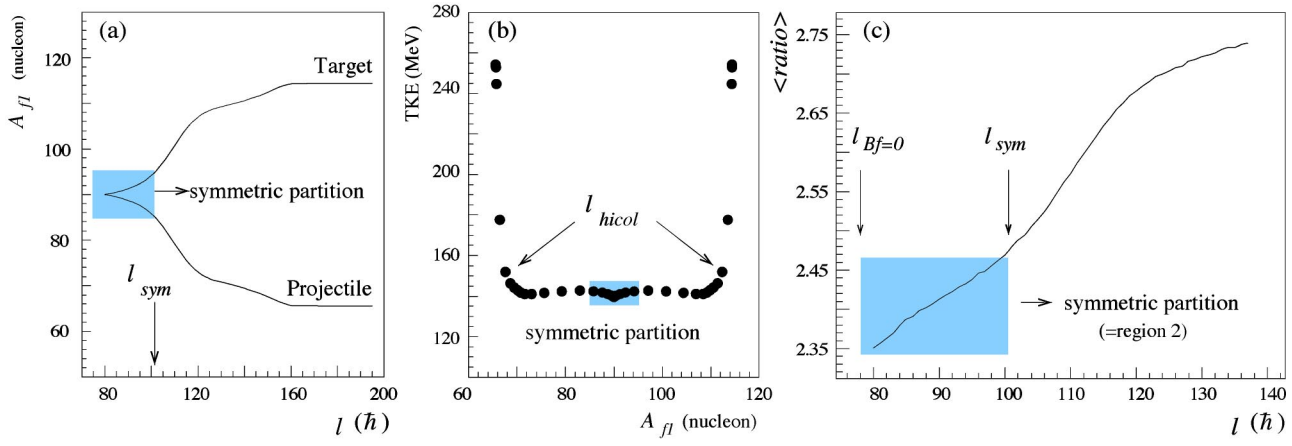

FIG. 13. (Color online) HICOL predictions for the (a) mass evolution of the reaction products as a function of the orbital angular momentum; (b) evolution of the TKE as a function of the angular momentum and the mass A_{f1} of one reaction product in the reaction ^{58}Ni(375.5 MeV)+^{122}Sn; (c) evolution of nuclear deformation of the composite system (mean ratio ⟨ratio⟩ of major to minor axes) as a function of the angular momentum.

TABLE V. Total fusion cross sections in barns measured in the experiments and predicted with HICOL and the static model of Wilcke [19].

Reaction	σ_{fusion} HICOL	σ_{fusion} Experimental	σ_{fusion} Static model
b375	1.47	1.50±0.13	0.82
b354	1.56		0.87
b382	1.45	1.45±0.13	0.94

and postscission multiplicities of all emitted light particles.

We have simulated our reactions with GEMINI only for symmetric fission ($A_{f1}=90\pm5$ nucleons). But, even in this case, the corresponding events are still mixed with DIC or fast fission [see Fig. 13(b)]. In order to take this into account, the simulations were separated in two regions (as already used in Ref. [16]). In the region 1, it was assumed that the CN is spherical for conventional fission which is allowed in the angular momentum range $\ell \leqslant \ell_{Bf=0}$ where $\ell_{Bf=0}$ is the angular momentum at which the fission barrier is predicted to vanish in the calculations of Sierk [20] (see Table I). The region 2 is associated to larger ℓ waves and the CN was assumed deformed for the DIC leading to quasisymmetric mass partition ($\ell_{Bf=0} \leqslant \ell \leqslant \ell_{sym}$) [see Fig. 13(a)].

In region 1, a standard statistical decay of the CN is modeled. The partial decay width for light-particle evaporation is calculated with the Hauser-Feshbach formalism using standard spherical transmission coefficients as in Ref. [31]. The fission decay width is calculated from the transition-state formalism using the angular-momentum-dependent fission barriers from Sierk [20]. By treating fission purely statistically, it has generally been found difficult to explain the large experimental prescission multiplicities of light particles in CN decay [32]. Therefore in order to simulate larger prescission emissions, dynamics are often introduced into the simulations. This consists of either a fission delay $\tau_d^{(1)}$, an initial time period where evaporation is allowed but fission is hindered due to the entrance-channel dynamics and the attainment of a thermal distribution of CN shapes, and/or by particle evaporation during the transition from the saddle point to the scission point. In these simulations we have chosen to model only the first of these and obtain $\tau_d^{(1)}$ from fitting the experimental data. As a simplification in the GEMINI simulations, the fission decay width is set to zero up to $\tau_d^{(1)}$ and then promptly assumes the transition-state value.

In region 2, a full treatment of fast fission or fully damped DIC would require a dynamical model which considers the variation of the shape of the composite system from the amalgamation of the projectile and target nuclei to the subsequent separation of the final fragments. During these dynamics, one should also allow for the evaporation of light particles. However, we have followed a simpler scheme which we believe captures the most important aspects of fast fission that relate to prescission and postscission evaporation. The evaporation from the composite system was treated as being from a deformed system of constant deformation which is meant to represent the mean shape of the system prior to scission. Based on the dynamical code HICOL [13], this shape was taken as prolate [with ratio of major to minor axes of 2.4 as shown in Fig. 13(c)] rotating about an axis perpendicular to its symmetry axis. Evaporation was considered for a time period of $\tau_d^{(2)}$ which is meant to represent the duration of the fast-fission interaction. Deformation energies, rotational energies, and transmission coefficients appropriate for the assumed deformation were used in the statistical-model simulations. For conventional and fast fission, the excitation energy at scission is divided between the two fission fragments and the postscission evaporation is simulated using spherical transmission coefficients.

TABLE VI. Values of the parameters a_f/a_n, $\tau_d^{(1)}$, and $\tau_d^{(2)}$ in zs obtained from fitting the experimental fusion-evaporation cross sections and the neutron prescission and postscission multiplicities introduced with the statistical-model code GEMINI.

	a_f/a_n	$\tau_d^{(1)}=\tau_d^{(2)}(10^{-21}\text{s})$
^{58}Ni+^{122}Sn at 375.5 MeV	1.17±0.03	70±5
^{58}Ni+^{122}Sn at 354 MeV	1.17±0.03	70±5
^{64}Ni+^{116}Sn at 382.5 MeV	1.13±0.03	40±5

In the GEMINI code three input parameters have been adjusted to reproduce our experimental data as follows.

(1) $\tau_d^{(1)}$ and $\tau_d^{(2)}$: fission dynamical delay times to be added to the lifetime of the CN before its scission.

(2) a_f/a_n: the ratio of the nuclear level density parameter at the saddle point to the level density parameter at equilibrium point (ground state).

The value of a_n in Eq. (9) was taken equal to $A/9$ MeV^{-1} and the initial excitation energy was assumed to correspond to the full momentum transfer reactions, i.e., complete fusion. In a pure and standard statistical-model code, the parameters should be $a_f/a_n=1$, $\tau_d=0$, and ratio=1. With slight modifications of this set of input parameters (for example: $a_f/a_n=1.05$, $\tau_d=0$, and ratio=1), GEMINI can successfully predict the experimental cross section σ_{er}. However, the predicted ν_n^{cn} values come out to be lower than 1 and therefore much smaller than the experimental values (see Table III) clearly justifying the introduction of fission dynamics. Moreover, to take into account the fast-fission processes, the simulated prescission and postscission multiplicities values are calculated as a weighted average:

$$\nu_i = \frac{\nu_i^{(1)}\sigma^{(1)} + \nu_i^{(2)}\sigma^{(2)}}{\sigma^{(1)} + \sigma^{(2)}}, \tag{15}$$

where $\nu_i^{(1)}$ and $\nu_i^{(2)}$ are the simulated multiplicity values from region (1) and (2), respectively. They are function of their corresponding dynamical delay time $\tau_d^{(1)}$ and $\tau_d^{(2)}$ and function of a_f/a_n. $\sigma^{(1)}$ and $\sigma^{(2)}$ are the cross sections associated with the two investigated ℓ regions. Following this procedure, the best parameters $\tau_d^{(1)}$, $\tau_d^{(2)}$, and a_f/a_n found to reproduce our experimental fusion-evaporation cross section and neutron prescission and postscission multiplicities were extracted. Their values are listed in Table VI. It appears that $\tau_d^{(2)}$ and a_f/a_n are very high compared with reported values in Ref. [16,33]. The effect of such a large value of a_f/a_n on the

fission cross section is equivalent to a decrease by 30% of the Sierk fission barriers used in the GEMINI code. In fact, such a decrease is needed to increase the fission probability of the CN and thus to reproduce our low experimental fusion-evaporation cross sections (50 mb). In the same way, $\tau_d^{(2)}$ had to be large in order to reproduce the large neutron multiplicities emitted from the deformed CN.

GEMINI is an efficient statistical-model code which can reproduce conventional and fast-fission data if parameters such as a_f/a_n and τ_d are modified to account for the dynamic aspects of the decay (see, for example: Refs. [16,24,29], and references therein). But, following our approach, we have not been able to reasonably reproduce our experimental values because the best fitted values of a_f/a_n and τ_d are too different from the normally expected values. Indeed, we must artificially increase the fission probability significantly and consequently the lifetime of the CN. This is apparently due to the presence of a significant deep-inelastic contribution, indistinguishable from fusion-fission events. Indeed, HICOL predicts that DIC are present in "symmetric fission" (see Fig. 13). This characteristic is more important when projectile and target have similar masses. This may be the reason why GEMINI reproduces very well experimental data for systems like ^{20}Ne+ ^{159}Tb and ^{169}Tm at comparable beam energies [16] but does not work reasonably for the Ni+Sn systems.

V. CONCLUSION

The cross sections of fusion-evaporation σ_{er} and fusion-fission σ_f have been measured for the two following reactions: ^{58}Ni+ ^{122}Sn at 375.5 MeV and ^{64}Ni+ ^{116}Sn at 382.5 MeV. The cross sections of fusion-fission σ_f obtained using detectors $R1$ and $R2$ or the MWPCs were in agreement, but clearly higher than the predictions based on the static fusion model of Wilcke [19]. These observations could be explained by the presence of deep inelastic events mixed with fission. Such an affirmation was demonstrated using the dynamical code HICOL [13].

As opposed to the fission fragments, the evaporation residues were well separated from the other processes. Using a simulation taking into account the angular and energy straggling of ions in the target, the cross sections of fusion evaporation σ_{er} were determined from a fit of the velocity distribution of the evaporation residues. The results, $\sigma_{er} = 50 \pm 8$ mb for both reactions, suggest no influence of the entrance channel on the competition between fusion-evaporation and fusion-fission around 6 MeV/nucleon. At energies near the Coulomb barrier, the results from Freeman *et al.* [5] indicated a larger σ_{er} for the ^{64}Ni+ ^{116}Sn reaction in favor of a neutron-skin effect at low bombarding energies. As a general conclusion, our results suggest that the neutron-skin effect on the fusion and on the competition between fusion-fission and fusion-evaporation disappears when the projectile energy largely exceed the Coulomb barrier.

The neutron multiplicities associated with the CN and the two FFs were determined using the DEMON multidetector array for fissionlike events. The results, $\nu_n^{cn} = 3 \pm 0.2$ and $\nu_n^{f1} = \nu_n^{f2} = 2 \pm 0.1$ for symmetric mass partition, indicate that there is no difference between the two reactions leading to the same CN with equal excitation energy, i.e., ^{58}Ni+ ^{122}Sn $\rightarrow$ ^{180}Pt ($E^* = 122$ MeV) and ^{64}Ni+ ^{116}Sn $\rightarrow$ ^{180}Pt ($E^* = 124$ MeV).

In conclusion, we can confirm that the decay of the CN, produced by these reactions, is completely independent from their entrance channels.

Therefore, at bombarding energies above the Coulomb barrier, there is no clear advantage of using either of the studied reactions to produce the compound nucleus. A skin effect could appear only at low energy or in more peripheral interactions such quasielastic processes.

To compare our complete set of data with theoretical values, the statistical code GEMINI was used [14]. The new version of this code takes into account the deformation effect on the CN decay. A set of initial parameters in the code allowed us to reproduce our experimental data. However, the fitted values, i.e., $a_f/a_n = 1.17$ and $\tau_d^{(2)} = 70$ *zs* in the reactions b354 and b382, are unexpectedly larger than previously published results [6,16]. This comes from the important presence of DIC in the fission events which was not well simulated by the code. This analysis suggests the need for a dynamic code such HICOL but taking into account the evaporation of light particles and the fission probabilities like GEMINI.

ACKNOWLEDGMENTS

The authors are indebted to the crew of Louvain-la-Neuve Cyclotron for the excellent and efficient running of the machine. We also thank P. Demaret for his important contributions to the target preparation. We wish to thank Dr. H. Feldmeier for making his code HICOL available to us. Some of us (R.C. and J.N.) would like to acknowledge the University of Louvain for its hospitality during their multiple stays in Belgium.

[1] N. Wang, X. Wu, and Z. Li, Phys. Rev. C **67**, 024604 (2003).
[2] G. A. Lalazissis, D. Vretenar, and P. Ring, Phys. Rev. C **57**, 2294 (1998).
[3] S. Ghosh, M. Nandy, P. K. Sarkar, and N. Chakravarty, Phys. Rev. C **49**, 1059 (1994).
[4] D. Vretenar, P. Finelli, A. Ventura, G. A. Lalazissis, and P. Ring, Phys. Rev. C **61**, 064307 (2000).
[5] W. S. Freeman, H. Ernst, D. F. Geesaman, W. Henning, T. J. Humanic, W. Khn, G. Rosner, J. P. Schiffer, B. Zeidman, and F. W. Prosser, Phys. Rev. Lett. **50**, 1563 (1983).
[6] K. T. Lesko, W. Henning, K. E. Rehm, G. Rosner, J. P. Schiffer, G. S. F. Stephans, and B. Zeidman, Phys. Rev. Lett.

55, 803 (1985).
[7] F. L. H. Wolfs, Phys. Rev. C **36**, 1379 (1987).
[8] A. M. van den Berg, W. Henning, L. L. Lee, Jr., K. T. Lesko, K. E. Rehm, J. P. Schiffer, G. S. F. Stephans, and F. L. H. Wolfs, Phys. Rev. Lett. **56**, 572 (1986).
[9] R. R. Betts *et al.*, Phys. Rev. Lett. **59**, 978 (1987).
[10] C. L. Jiang, K. E. Rehm, H. Esbensen, D. J. Blumenthal, B. Crowell, J. Gehring, B. Glagola, J. P. Schiffer, and A. H. Wuosmaa, Phys. Rev. C **57**, 2393 (1998).
[11] H. Esbensen, C. L. Jiang, and K. E. Rehm, Phys. Rev. C **57**, 2401 (1998).
[12] V. Roberfroid, Ph.D. thesis, Université catholique de Louvain, 2003.
[13] H. Feldmeier, Rep. Prog. Phys. **50**, 915 (1987).
[14] R. J. Charity, Nucl. Phys. **A457**, 441 (1986).
[15] S. Kaufman, E. Steinberg, B. Wilkins, J. Unik, A. Gorki, and M. Fluss, Nucl. Instrum. Methods **115**, 47 (1974).
[16] J. Cabrera *et al.*, Phys. Rev. C **68**, 034613 (2003).
[17] I. Tilquin *et al.*, Nucl. Instrum. Methods Phys. Res. A **365**, 446 (1995).
[18] H. Morgenstern, Z. Phys. A **313**, 39 (1983).
[19] W. W. Wilcke, J. R. Birkelund, H. J. Wollersheim, A. D. Hoover, J. R. Huizenga, W. U. Schröder, and L. E. Tubbs, At. Data Nucl. Data Tables **25**, 389 (1980).
[20] A. J. Sierk, Phys. Rev. C **33**, 2039 (1986).
[21] B. Borderie, M. Berlanger, D. Gardès, F. Hanappe, L. Nowicki, S. Agarwal, J. Girard, C. Grégoire, J. Matuszek, and C. Ngô, Z. Phys. A **299**, 263 (1981).
[22] L. Tassan-Got and C. Stéphan, Nucl. Phys. **A524**, 121 (1991).
[23] H. Rossner, D. Hilscher, D. J. Hinde, B. Gebauer, M. Lehmann, M. Wilpert, and E. Mordhorst, Phys. Rev. C **40**, 2629 (1989).
[24] R. J. Charity *et al.*, Phys. Rev. C **67**, 044611 (2003).
[25] L. C. Vaz and J. M. Alexader, Z. Phys. A **318**, 213 (1985).
[26] M. Gonin *et al.*, Nucl. Phys. **A495**, 139c (1989).
[27] K. Siwek-Wilczynska, J. Wilczynski, H. K. W. Leegte, R. H. Siemssen, and H. W. Wilschut, Phys. Rev. C **48**, 228 (1993).
[28] B. J. Fineman, K.-T. Brinkmann, A. L. Caraley, N. Gan, R. L. McGrath, and J. Velkovska, Phys. Rev. C **50**, 1991 (1994).
[29] R. J. Charity *et al.*, Phys. Rev. C **63**, 024611 (2001).
[30] G. Viesti *et al.*, Phys. Lett. B **521**, 165 (2001).
[31] R. J. Charity, M. Korolija, D. G. Sarantites, and L. G. Sobotka, Phys. Rev. C **56**, 873 (1997).
[32] D. Hilscher and H. Rossner, Ann. Phys. (Paris) **17**, 471 (1992).
[33] J. O. Newton, D. G. Popescu, and J. R. Leigh, Phys. Rev. C **42**, 1772 (1988).